Atmospheric scattering of energetic electrons from near-Earth space

V. Angelopoulos[1*], E. Tsai[1], C. Wilkins[1], X.-J. Zhang[1], A. V. Artemyev[1], J. Liu[1], A. Runov[1], L. Iglesias[1], D. L. Turner[2], R. J. Strangeway[1], R. E. Wirz[3], W. Li[4], L. Adair[1,5], R. P. Caron[1], M. Chung[2], P. Cruce[6], E. Grimes[1], K. Hector[7], M. J. Lawson[1], D. Leneman[1], E. V. Masongsong[1], A. Norris[1], C. L. Russell[1], C. Shaffer[8], J. Wu[1], S. Jha[1,9], J. King[1,9], S. Kumar[1,10], K. Nguyen[1,3], M. Nguyen[1,11], A. Palla[1,9], A. Roosnovo[1,10], E. Xie[1,11], R. Yap[1,12], C. Young[1,9], J. B. Blake[13], N. Adair[5], M. Allen[14], M. Anderson[15], M. Arreola-Zamora[1,14], J. Artinger[1,10], J. Asher[2], D. Branchevsky[13], M. R. Capitelli[5], R. Castro[7,9], G. Chao[3,16], N. Chung[17], M. Cliffe[18], K. Colton[19], C. Costello[20], D. Depe[11], B. W. Domae[11], S. Eldin[11], L. Fitzgibbon[8], A. Flemming[14], I. Fox[3], D. M. Frederick[5], A. Gilbert[11], A. Gildemeister[14], A. Gonzalez[9], B. Hesford[21], R. Krieger[22], K. Lian[14], J. Mao[23], E. McKinney[24], J. P. Miller[9], M. Nuesca[9], E. S. Y. Park[25], C. E. Pedersen[3], Z. Qu[3], R. Rozario[18], E. Rye[11], R. Seaton[1], A. Subramanian[14], S. R. Sundin[8], A. Tan[26], W. Turner[10], A. J. Villegas[10], M. Wasden[3], G. Wing[9], C. Wong[10], A. Zarifian[21], G. Y. Zhang[27]

Affiliations:

1 Earth, Planetary, and Space Sciences Department, and Institute of Geophysics and Planetary Physics, University of California, Los Angeles, CA 90095
2 Johns Hopkins University Applied Physics Laboratory, Laurel, Maryland 20723
3 Mechanical and Aerospace Engineering Department, Henry Samueli School of Engineering, University of California, Los Angeles, CA 90095
4 Department of Astronomy and Center for Space Physics, Boston University, Boston, MA 02215
5 Millenium Space Systems, El Segundo, CA 90245
6 Apple Inc., Cupertino, CA 95014
7 Raytheon Space and Airborne Systems, El Segundo, CA 90245
8 Tyvak Nano-Satellite Systems, Inc., Irvine, CA 92618
9 Computer Science Department, Henry Samueli School of Engineering, University of California, Los Angeles, CA 90095
10 Physics and Astronomy Department, University of California, Los Angeles, CA 90095
11 Electrical and Computer Engineering Department, Henry Samueli School of Engineering, University of California, Los Angeles, CA 90095
12 Mathematics Department, University of California, Los Angeles, CA 90095
13 The Aerospace Corporation, El Segundo, CA 90245
14 Northrop Grumman Aerospace Systems, Redondo Beach, CA 90278
15 Lucid Motors, Newark, CA 94560
16 Boeing, El Segundo, CA 90245
17 Tesla, Palo Alto, CA 94306
18 SpaceX, Hawthorne, CA 90250
19 Planet Labs, San Francisco, CA 94107
20 NovaSignal, Los Angeles, CA 90064
21 Jet Propulsion Laboratory, Pasadena, CA 91109
22 Mercedes-Benz Research and Development North America, Long Beach, CA 90810
23 Epic Systems Corporation, Verona, WI 53593
24 California State Polytechnic University, Pomona, CA 91768
25 Economics Department, University of California, Los Angeles, CA 90095
26 Experior Laboratories, Oxnard, CA 93033
27 Qualcomm, San Diego, CA 92121

[*]Correspondence to: vassilis@ucla.edu

Summary paragraph:

In near-Earth space, the magnetosphere, energetic electrons (tens to thousands of kiloelectron volts) orbit around Earth, forming the radiation belts. When scattered by magnetospheric processes, these electrons precipitate to the upper atmosphere, where they deplete ozone, a radiatively active gas, modifying global atmospheric circulation. Relativistic electrons (those above a few hundred kiloelectron volts), can reach the lowest altitudes and have the strongest effects on the upper atmosphere; their loss from the magnetosphere is also important for space weather. Previous models have only considered magnetospheric scattering and precipitation of energetic electrons; atmospheric scattering of such electrons has not been adequately considered, principally due to lack of observations. Here we report the first observations of this process. We find that atmospherically-scattered energetic (relativistic) electrons form a low-intensity, persistent "drizzle", whose integrated energy flux is comparable to (greater than) that of the more intense but ephemeral precipitation by magnetospheric scattering. Thus, atmospheric scattering of energetic electrons is important for global atmospheric circulation, radiation belt flux evolution, and the repopulation of the magnetosphere with lower-energy, secondary electrons.

Main article: Polar ozone exerts strong radiative forcing on global atmospheric circulation by modifying temperature, winds, and waves in the upper atmosphere. Energetic electrons from near-Earth space can reach the high-latitude mesosphere (50-100km), where they produce reactive odd nitrogen and hydrogen (NO_x and HO_x), ozone-destroying catalysts. Nitrogen oxides can also descend to the stratosphere (25-50km), where they become the most important contributors to catalytic ozone destruction. Thus, energetic electron precipitation can affect the global ozone cycle[1,2,3] and global circulation significantly. Despite their importance for modeling atmospheric circulation, energetic particles have not been adequately incorporated into global atmospheric models[4,5,6], resulting in large discrepancies between model predictions and observations of vertical ozone profiles[7]. Magnetospheric energetic electrons (especially relativistic ones) are also important for space weather, as they can damage satellites and harm astronauts, particularly during magnetic storms[8,9]. Their fluxes, a delicate balance of large contributions from transport, acceleration, and loss, vary so as to defy predictability by modeling. These electrons can be trapped for hours to weeks in the outer radiation belt, which is near the magnetic equator at geocentric distances of L=3-7 Earth radii. Plasma waves[10] or extreme equatorial field-line curvature[11] can scatter them, reducing their velocity angle (pitch angle, α) relative to the magnetic field, **B**, to less than the loss cone angle ($\alpha<\alpha_{LC}$). This allows them to reach the mesosphere or stratosphere, where they collide, deposit their energy and are lost from the magnetosphere. Although magnetospheric scattering has been incorporated into radiation belt diffusion models[12,13], because of lack of observations, atmospheric scattering has not, resulting in significant model deficiencies[14,15]. Using the first low-altitude (~410km), high-resolution (in both pitch angle and energy) observations of energetic (50-5800keV) electrons by the ELFIN mission[16], we report on atmospheric scattering and its dependence on activity and location. We interpret upgoing electrons ($180^o-\alpha_{LC}<\alpha$) at some energy, E, as secondary electrons produced by atmospheric scattering of either trapped (α~90^o) or precipitating ($\alpha<\alpha_{LC}$) primary electrons of a greater energy. (Note: unless otherwise stated, pitch angles are referenced to the northern hemisphere; for the southern hemisphere, use their supplementary). We find that the net energetic (relativistic) electron energy flux precipitation from atmospheric scattering is comparable to (greater than) that from magnetospheric scattering.

ELFIN, a dual CubeSat, polar-orbiting mission launched in 2018, has collected data from >1000 science zones (magnetically mapping to L=2-15), covering all local times and a wide range of geomagnetic conditions. We use energetic particle detector instrument (EPDE) data obtained by ELFIN-A (EL-A) from magnetic local times within $\pm$4 hours of the noon-midnight plane between 2019/09/01 2020/11/13 (~700 science zones). The instrument has a single square-aperture field-of-view (FOV=22^{o}). Spinning on a plane containing **B**, once per spin (~3sec) it provides 15 energy channels (50keV-5800keV) of width ΔE/E~40% and 16 spin-phase sectors of width SCW=22.5^{o}. Spin-phases are transformed to pitch-angles using the international geophysical reference field (IGRF) model. At ELFIN's altitude, the loss cone is α_{LC}~67$^{o}\pm$2^{o}. Precipitating (downgoing) or atmospherically-scattered (upgoing) electrons were measured when the detector's full width (FOV+SCW) was entirely within the loss cone or the anti-loss cone, respectively. Trapped electrons had sector centers α=90$^{o}\pm$11.25^{o}.

Atmospheric scattering of precipitating electrons ("backscatter") should produce low upgoing-to-downgoing ratios[15]. Thus, when magnetospherically scattered precipitation is significant (relative to trapped fluxes), atmospheric backscatter should yield low upgoing-to-downgoing flux ratios. Atmospheric scattering of (barely) trapped electrons should result in low (relative to trapped) but balanced upgoing and downgoing fluxes at upper atmospheric altitudes (upgoing-to-downgoing ratios ~100%). Thus, when magnetospherically-scattered precipitation (and, consequently, its atmospheric backscattering) is low, atmospheric scattering of trapped fluxes can dominate, resulting in upgoing-to-downgoing flux ratios ~100% *at the upper atmosphere*. Under such conditions, the absence of magnetospheric scattering sites near the equator should allow atmospherically-scattered upgoing energetic electrons from the opposite hemisphere to be detected at the local hemisphere as downgoing, resulting in upgoing-to-downgoing ratios ~100% *also at the satellite*.

ELFIN-A observations of a northern, nightside (MLT~1) science zone (Figure 1a) during an active time (the D_{ST} index[17] had a minimum of -49nT fourteen hours earlier[18]) confirms the above expectations from atmospheric scattering. Significant downgoing fluxes ($\alpha<\alpha_{LC}$) are evident between L=3.5 and 6.5 (Figure 1b-c). When the downgoing energy flux (precipitation) was a large fraction of the trapped flux (as between 13:13:00 and 13:15:00UT, Figure 1f,h), the upgoing ($180^o-\alpha_{LC}<\alpha$) flux intensified, too (Figure 1d), but remained lower than the precipitation (upgoing-to-downgoing ratio was a few percent, Figure 1i). Conversely, when the precipitation was low, only a few percent of the trapped flux (as between 13:11:50 and 13:12:20UT, Figure 1f,h), the upgoing flux was also low (Figure 1d), but comparable to the precipitation (up-to-down flux ratio ~100%, Figure 1i).

When intense precipitation from magnetospheric scattering occurs up to some maximum energy, E_{pmax}, atmospheric scattering above E_{pmax} is expected continue to be dominated by atmospheric electron scattering at both hemispheres (upgoing-to-downgoing ratio ~100%), impervious to magnetospheric scattering and its atmospheric feedback below E_{pmax}. Indeed, this can be seen at ~13:12:35UT, when the downgoing-to-perpendicular ratio (Figure 1h) was elevated (~50%) at $E<E_{pmax}$~500keV: while the upgoing-to-downgoing ratio (Figure 1i) was suppressed (~30%) at $E<E_{pmax}$, it remained ~100% at $E>E_{pmax}$. Subsequently, as

E_{pmax} increased progressively from 150keV to 800keV (13:12:45-13:13:15UT, Figure 1h), the energy where the upgoing-to-downgoing ratio transitioned from low (<10%) to high (>60%) values followed E_{pmax} (Figure 1i), as expected. Additional examples are shown in Extended Data Figures 1 and 2 (nightside and dayside, respectively). Therefore, atmospheric scattering of trapped fluxes is quantifiable and long-lasting, based on case studies.

Atmospheric scattering of intense, high-energy precipitation is also expected to create copious backscattered electrons at $E \ll E_{pmax}$. Indeed, at 13:13:10–13:14:00UT, when the downgoing-to-perpendicular ratio is high, ~100%, with E_{pmax}~1MeV (Figure 1h), the upgoing-to-downgoing flux ratios are low (~1-2%) near E_{pmax} (Figure 1i), but are significant (20-50%) at energies several times lower than E_{pmax} (50-150keV). Another example is in Extended Data Figure 1 (13:47:15–13:47:30UT). Thus, atmospheric scattering of precipitation can also be a significant source of energetic electrons in the magnetosphere, as previously suggested[14,15].

Henceforth we refer to atmospheric scattering of trapped fluxes (upward or downward) as "energetic electron drizzle" and to atmospheric scattering of magnetospheric precipitation (upward only) as "energetic electron backscatter". Upgoing secondary electrons can be produced by either (generally both). Likewise, downgoing (or "precipitating") energetic electrons can be from either downward drizzle (even from the opposite hemisphere) or magnetospheric precipitation (originating from magnetospheric scattering even after subsequent backscatter at the opposite hemisphere).

To further quantify the importance of atmospheric scattering, we employ broad-energy flux channels LoE (50-430keV) and HiE (430-5800keV) in the upgoing, downgoing and perpendicular directions (f_u, f_d, $f_\perp$, respectively), and statistically significant flux ratios within each channel RLoE, RHiE (f_u/f_d, $f_d/f_\perp$, $f_u/f_\perp$, with relative error <50%), as in Figure 1j-m (and Extended Data Figures 1I-L, 2I-L). These form the basis of our statistical analysis, below. (Materials and Methods and Extended Data Figure 3 detail how these were constructed).

Medians of the above ratios at the nightside (Figure 2b,d) exhibit L-shell variations familiar from the nightside time series examined previously (Figure 1; Extended Data Figure 1): at low L-shells, atmospheric drizzle dominates ($f_d/f_\perp$<10%; f_u/f_d~70-100%); at high L-shells, magnetospheric precipitation dominates ($f_d/f_\perp$>40%; f_u/f_d~10%). The transition L-shell decreases with geomagnetic activity (based on the Auroral Electrojet index AE[17,18]). This is consistent with an equatorward motion of the equatorward edge of the auroral oval (where intense plasma waves and field-line scattering sites responsible for magnetospheric scattering map), typical during active times[19]. At the dayside (Figure 2a,c), precipitation is dominated by drizzle (as in Extended Data Figure 2). The statistical behavior of our dataset is thus expected to be bimodal, with a drizzle-dominated subset at low L-shells and a magnetospheric precipitation-dominated subset at high L-shells.

And, indeed, probability density functions (PDFs) in $(f_d+f_u)/f_\perp$-space (Figure 3a) reveal two peaks: The low-precipitation PDF peak ($(f_d+f_u)/f_\perp$~2-10%) has f_u/f_d~100%, corresponds to the low L-shells in Figures 1 and 2 (also Extended Data Figures 1 and 2), and is identified as atmospheric drizzle. The high-precipitation PDF peak ($(f_d+f_u)/f_\perp$~100%) has f_u/f_d~7$\pm$3%, corresponds to the high L-shells in the above figures, and is identified as enhanced precipitation mostly due to magnetospheric scattering.

Precipitation of 50-430keV (LoE) electrons (Figure 3c) is dominated by intense magnetospheric scattering (mostly by plasma waves), which overcomes the more common but lower-intensity drizzle. Precipitation of 430-5800keV (HiE) and 50-5800keV (integral channel) electrons is also dominated by magnetospheric scattering, but exhibits a significant contribution from drizzle. Upgoing fluxes also exhibit a similar bimodal behavior (Figure 3b). At all channels (LoE, HiE and integral), the drizzle peak ($(f_d+f_u)/f_\perp$~2-10%) dominates the upgoing flux. However, the magnetospheric precipitation peak ($(f_d+f_u)/f_\perp$~100%), corresponding mostly to backscatter (though likely some upward drizzle, too), also contributes significantly to the LoE channel. These peaks and their properties remain similar when examined as a function of $f_\perp$ (Extended Data Figure 4) and geomagnetic activity and for the subset of the outer radiation belt ($3<L<7$).

Evaluation of atmospheric scattering's net impact on precipitation starts from Table 1, showing the measured upgoing-to-downgoing flux ratios, $r=<f_u>/<f_d>$, separately for the nightside, dayside and combined. We see that r~45% for HiE and r~18% for the integral channel.

Next, we recall that the downgoing flux contribution from scattering below the satellite cannot be measured directly; it must be inferred. We note that the upgoing HiE and integral flux (Figure 3b) are dominated by upward drizzle, f_a (main peak, and likely a good part of the secondary peak), which is up-down symmetric and occurs at both atmospheric feet of a field line. It is therefore a good proxy for the downward drizzle arriving from the opposite hemisphere. The measured downgoing flux for the HiE and integral channels (Figure 3c) is supplied by both magnetospheric precipitation, f_m, and downward drizzle from the opposite hemisphere, f_a. Thus, at ELFIN, to zero order, we measure (Table 1): $r=<f_u>/<f_d>\sim f_a/(f_a+f_m)$. The atmospheric scattering contribution to precipitation is $\sim 2f_a$, the total precipitation at each hemisphere is $\sim 2f_a+f_m$, and the relative contribution of atmospheric scattering to precipitation is $R=2f_a/(2f_a+f_m)$. If $x=2f_a/f_m$ (atmospheric relative to magnetospheric scattering), using $r=x/(x+2)$ and the measured values of r (Table 1), we find x=161%, $R=1/(1+x)\sim 62\%$ for HiE, and x~45%, R~31% for the integral channel. For the outer radiation belt ($3<L<7$) during all activity levels and during only active times ($D_{ST}<-20$nT), we obtain (Extended Data Table 1) similar values, though somewhat reduced due to the increased relative contribution of magnetospheric precipitation in those subsets.

Thus, atmospheric scattering contributes more than magnetospheric scattering to the precipitation energy at relativistic energies (>430keV) and as much as 45% of the magnetospheric precipitation at energies >50keV. Since relativistic electrons can reach the upper/middle stratosphere, resulting in very efficient catalytic ozone depletions, and are also a critical contributor to space weather, our results necessitate a factor of ~2 upwards revision of energy flux inputs in atmospheric models and energy flux losses in radiation belt models. Moreover, during intense magnetospheric precipitation, the backscattered energetic electron energy flux at low energies is a significant fraction of both precipitating and trapped flux. Thus, atmospheric scattering can be also important for seeding the radiation belts with electrons and for generating plasma waves; its effects need to be further quantified with observationally-driven modeling.

Data availability statement

ELFIN data are available through http://elfin.igpp.ucla.edu.

Code availability statement

ELFIN mission data have been imported, analyzed, and plotted using corresponding plug-ins to the open-source SPEDAS analysis platform[20] (http://spedas.org).

Supplementary Information is linked to the online version of the paper at www.nature.com/nature.

Acknowledgments: We acknowledge support by NASA award NNX14AN68G (5/22/2014 – present) and NSF awards # AGS-1242918 (9/24/2014-7/31/2019) and AGS-2019950 (July 2020 – present). We are grateful to NASA's CubeSat Launch Initiative program for successfully launching the ELFIN satellites in the desired orbits under ELaNa XVIII. We thank the AFOSR for early support of the ELFIN program under its University Nanosat Program, UNP-8 project, contract # FA9453-12-D-0285 (02/01/2013-01/31/2015). We also thank the California Space Grant program for student support during the project's inception (2010-2014). We acknowledge the hardware contributions and technical assistance of Mr. David Hinkley and The Aerospace Corporation. We thank V. A. Sergeev, Y. A. Shprits and W. Greer for useful discussions in the early stages of the program. We acknowledge the critical contributions of the many volunteer ELFIN team members (more than 250 students). We thank Ms. J. Hohl for editorial assistance with the manuscript.

244 **Figure 1a**

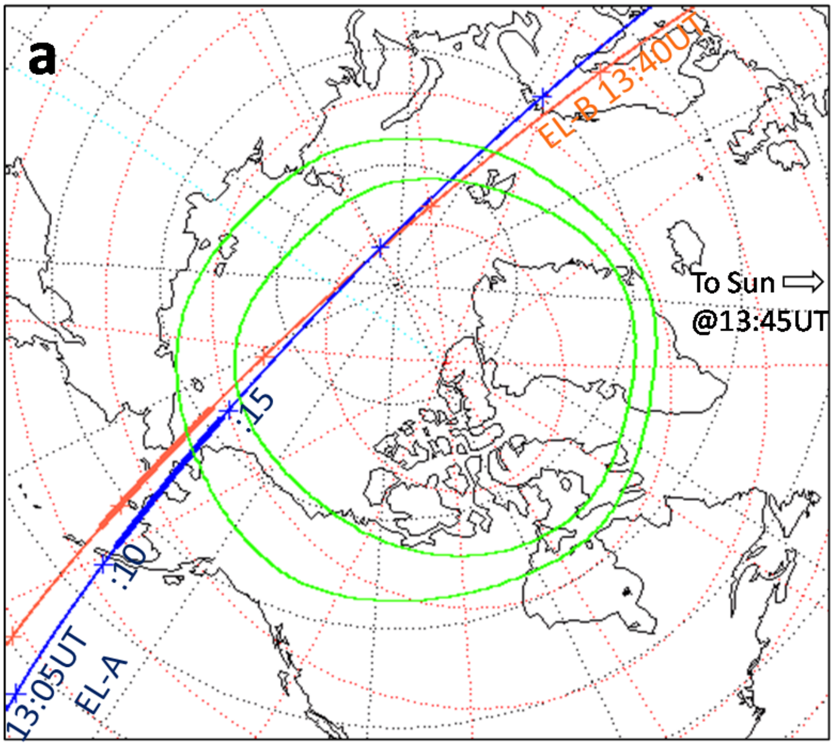

245

246

Figure 1b-m

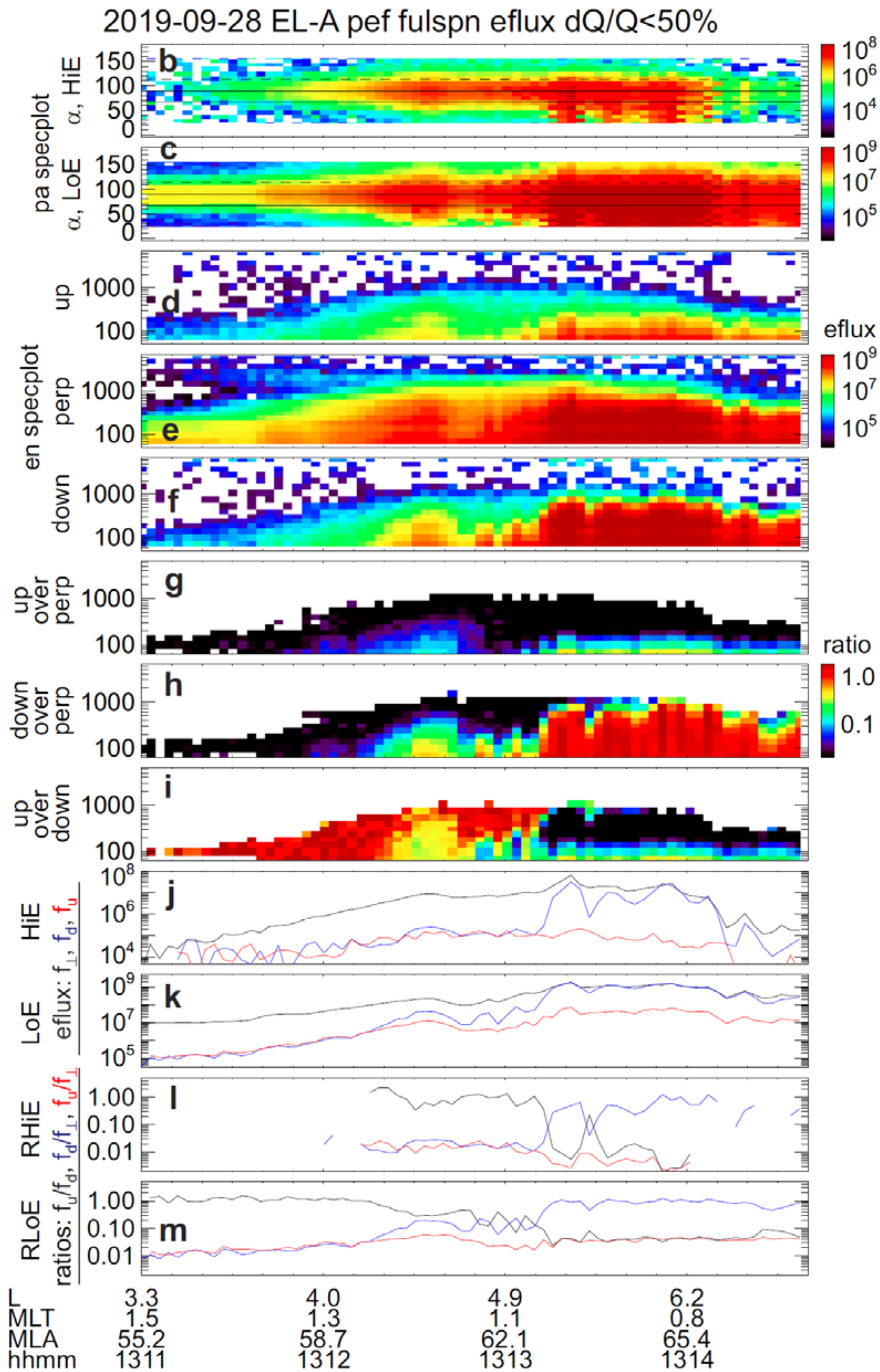
2019-09-28 EL-A pef fulspn eflux dQ/Q<50%
pa specplot
α, HiE
α, LoE
en specplot
up
perp
down
eflux
up over perp
down over perp
up over down
ratio
HiE
LoE
eflux: f⊥, fd, fu
RHiE
RLoE
ratios: fu/fd, fd/f⊥, fu/f⊥
b
c
d
e
f
g
h
i
j
k
l
m
L 3.3 4.0 4.9 6.2
MLT 1.5 1.3 1.1 0.8
MLA 55.2 58.7 62.1 65.4
hhmm 1311 1312 1313 1314

Figure 1 | ELFIN storm-time, nightside crossing of the outer radiation belt and auroral zone. (**a**) EL-A satellite track geographic projections (fixed at 13:45UT) on 28 September 2019. Thick lines represent times of data capture; 5-min intervals are indicated by crosses. Black (red) dotted lines are geographic (corrected geomagnetic) meridians and parallels. Green lines are nominal auroral oval boundaries. (**b**-**c**) Pitch-angle spectrograms of differential directional energy flux ("energy flux" in keV/cm^{2}s str MeV) in broad-energy electron channels HiE and LoE (430-5800keV and 50-430keV energies, respectively). Bottom solid and upper dashed horizontal lines in each spectrogram mark the loss cone ($\alpha=\alpha_{LC}$) and anti-loss cone ($\alpha=180^o-\alpha_{LC}$); middle solid line denotes $\alpha=90^o$. (**d**-**f**) Energy-time spectrograms of upgoing (within anti-loss cone: $\alpha>180^o-\alpha_{LC}$), nearly-perpendicular to **B** (trapped), and downgoing (within loss cone: $\alpha<\alpha_{LC}$) electron energy flux. The energy ranges from 50keV to ~5800keV. (**g**-**i**) Energy-time spectrograms of upgoing-to-perpendicular (up-to-perp, $f_u/f_\perp$), downgoing-to-perpendicular (down-to-perp, $f_d/f_\perp$), and upgoing-to-downgoing (f_u/f_d) electron energy flux. (**j**-**k**) Energy flux in channels HiE and LoE (black: $f_\perp$; blue: f_d; red: f_u). (**l**-**m**) Ratios of energy flux in channels HiE and LoE, respectively (black: f_u/f_d; blue: $f_d/f_\perp$; red: $f_u/f_\perp$). Annotations denote L-shell (L), dipole magnetic local time (MLT), dipole magnetic latitude (MLA) and Universal Time (UT).

268 **Figure 2**

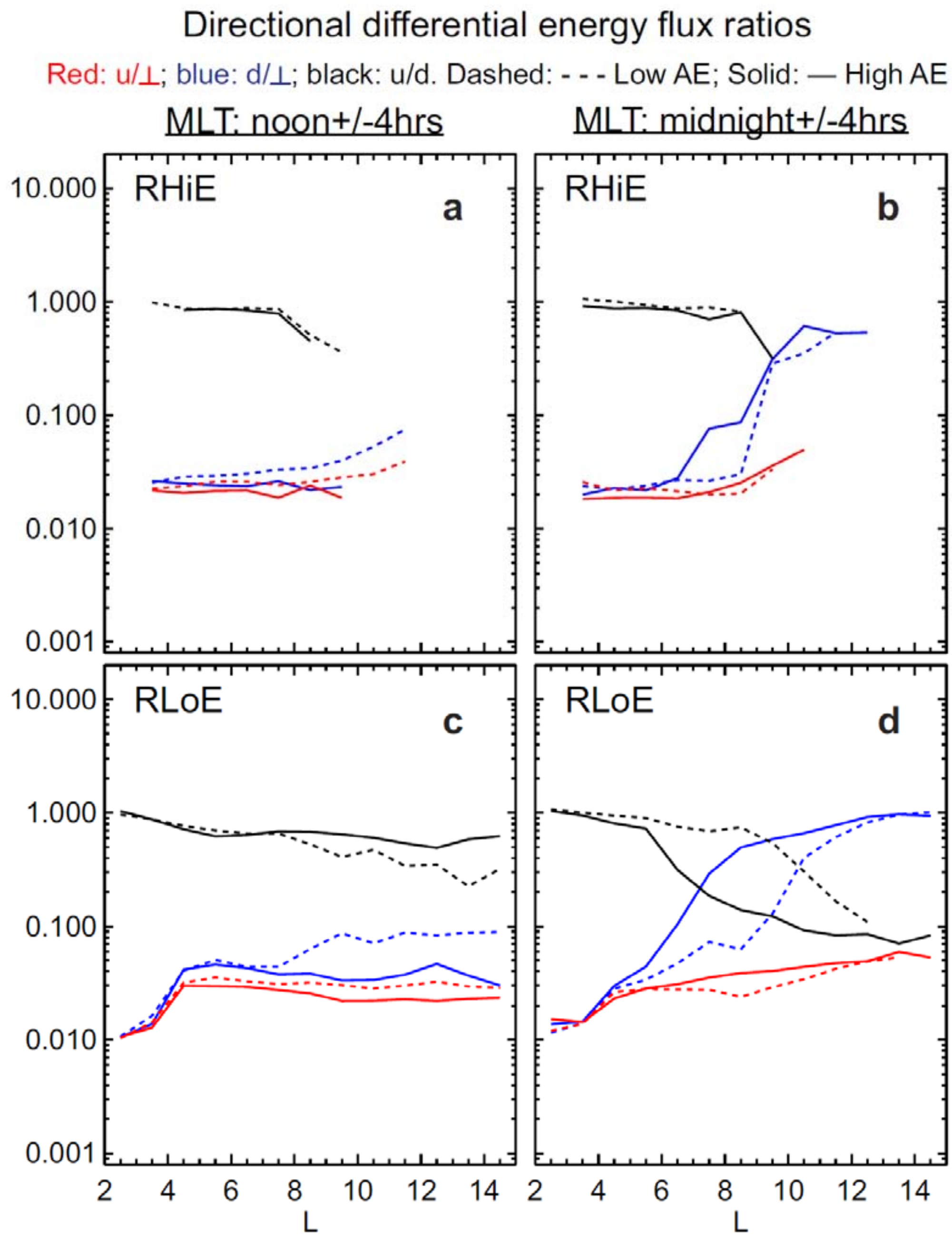

269

270

Figure 2 | Dependence of energy flux ratios on L-shell, local time, and activity. (**a-d**) Medians of ratios: $f_u/f_\perp$ (red), $f_d/f_\perp$ (blue), f_u/f_d (black) as a function of L-shell. Top and bottom panels: I430 and I50 energy channels, respectively. Left and right panels: dayside and nightside, respectively. Dashed and solid lines: data correspond to below and above the median AE, respectively. (AE medians for dayside and nightside databases are: 110nT and 160nT, respectively).

Figure 3

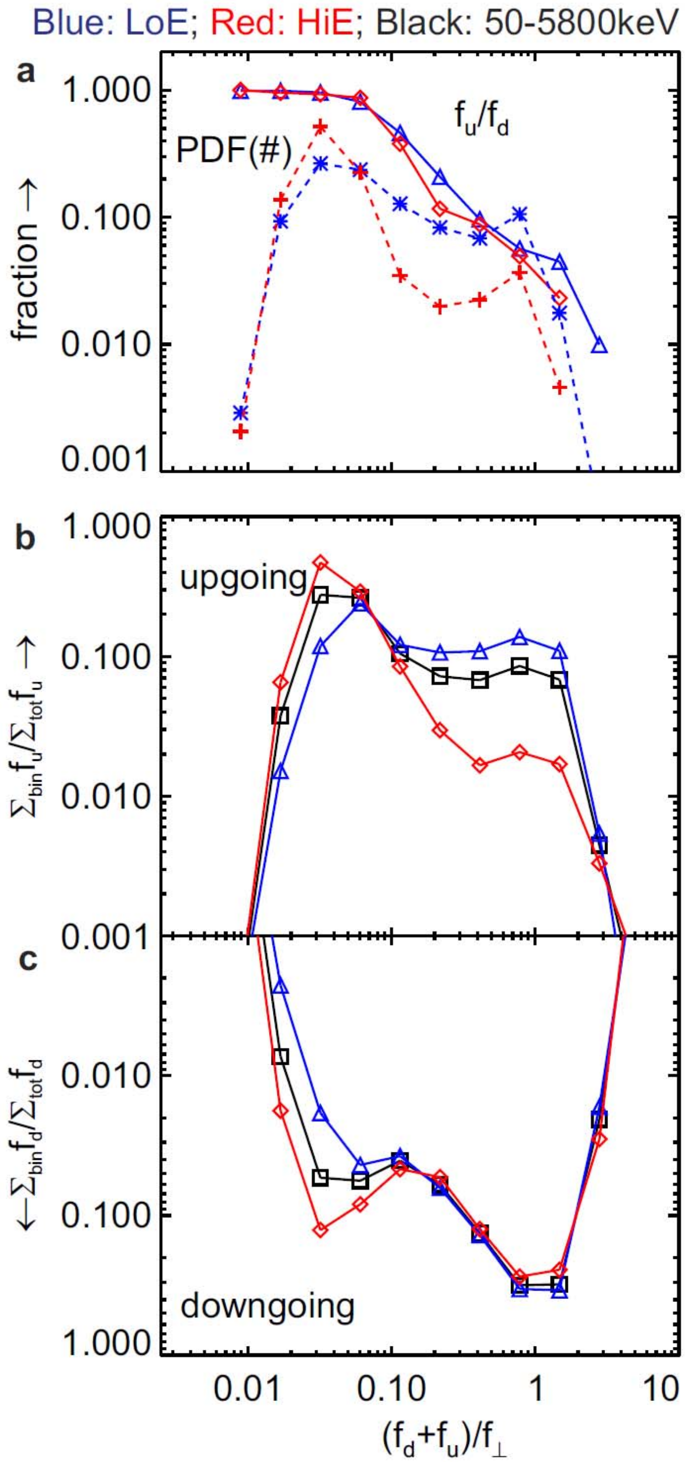
Blue: LoE; Red: HiE; Black: 50-5800keV
a
b
c
fraction →
f_u/f_d
PDF(#)
upgoing
downgoing
Σ_bin f_u/Σ_tot f_u →
← Σ_bin f_d/Σ_tot f_d
1.000
0.100
0.010
0.001
0.01
0.10
1
10
(f_d+f_u)/f_⊥

Figure 3 | Distribution of data, fluxes, and flux ratios as a function of loss-cone flux. (**a**) Probability density functions of all data in the I50 and I430 channels (blue stars and red crosses, respectively) and medians of flux ratios (f_u/f_d) for these channels (blue triangles and red diamonds, respectively). (**b**) Relative contribution to net upward flux within the I50 and I430 broad differential broad energy channels (blue triangles and red diamonds, respectively) and within the summed energy channel representing the total energy flux measured by the detector, i.e., at energies 50 keV – 5.8 MeV (black squares). (**c**) Same as in (**c**) but for the downward flux. Two-dimensional versions of several of these distributions, also plotted against the perpendicular energy flux, are shown in Extended Data Figure 4.

Table 1

<table>
<tr><th colspan="8">Average Directional Electron Fluxes† and their Measured Ratios (all data, 2<L<15)</th></tr>
<tr><th>MLT</th><th>Energy [keV]</th><th>r=<f_u>/<f_d></th><th><f_d>/<$f_\perp$></th><th colspan="2"><$f_\perp$> [Units]</th><th colspan="2" rowspan="2">Inferred‡ Ratios</th></tr>
<tr><td rowspan="2">Night</td><td>LoE: 50-430</td><td>9.4%</td><td>39.1%</td><td>1.28E+07</td><td rowspan="6">keV/cm^2 s str MeV (Differential Directional Energy Flux)</td></tr>
<tr><td>HiE: 430-5800</td><td>36.9%</td><td>9.8%</td><td>1.17E+06</td><td rowspan="4">x=2fa/fm</td><td rowspan="4">R= 2fa/(2fa+fm)</td></tr>
<tr><td rowspan="2">Day</td><td>LoE: 50-430</td><td>14.2%</td><td>25.1%</td><td>6.96E+06</td></tr>
<tr><td>HiE: 430-5800</td><td>80.3%</td><td>6.1%</td><td>4.11E+05</td></tr>
<tr><td rowspan="3">Night+Day, Residence-time Norm'ed</td><td>LoE: 50-430</td><td>10.6%</td><td>34.2%</td><td>9.88E+06</td></tr>
<tr><td>HiE: 430-5800</td><td>44.7%</td><td>8.9%</td><td>7.89E+05</td><td>161%</td><td>62%</td></tr>
<tr><td>50-5800 (Integral)</td><td>18.3%</td><td>20.8%</td><td>7.99E+06</td><td>keV/cm^2 s str</td><td>45%</td><td>31%</td></tr>
</table>

†Noise subtracted: $f_{n.HiE}$=3.48 10^3, $f_{n.LoE}$=2.74 10^3 [keV/cm^2 s str MeV] ‡where R=x(x+1); r=x/(x+2)

Table 1 | Differential and integral directional energy fluxes and ratios under all geomagnetic conditions, local times and latitudes in our database (2<L<15). Ratios of time averages rather than medians of ratios have been used, to accurately characterize total energy flux ratios. Night+Day ratios were computed directly from the numbers above them, assuming equal satellite residence time at day and night. Bottom row, which represents the integral directional energy flux channel (50-5800keV), was computed directly from the rows above it. f_u and f_d are upgoing and downgoing fluxes, <> represents average, and f_a and f_m are the measured contributions to precipitation from atmospheric scattering and magnetospheric scattering. The ratios x and R are the inferred net contributions to precipitation from atmospheric scattering relative to magnetospheric scattering and relative to the total precipitation, respectively.

Supplementary Information:

Methods

Extended Data Figures 1 - 4

Extended Data Table 1

References

[1] Jackman, C. H., Frederick, J.E. & Stolarski, R.S. Production of odd nitrogen in the stratosphere and mesosphere: An intercomparison of source strengths. *J. Geophys. Res., Oceans*. **85**, C12, 7495-7505 https://doi.org/10.1029/JC085iC12p07495 (1980).

[2] Thorne, R.M. The importance of energetic particle precipitation on the chemical composition of the middle atmosphere. *PAGEOPH* **118**, 128–151 https://doi.org/10.1007/BF01586448 (1980).

[3] Randall, C.E. et al. Stratospheric effects of energetic particle precipitation in 2003–2004. *Geophys. Res. Lett.* **32**, 5, https://doi.org/10.1029/2004GL022003 (2005).

[4] Baker, D.N. et al. Highly relativistic magnetospheric electrons: A role in coupling to the middle atmosphere? *Geophys. Res. Lett*. **14**, 10 https://doi.org/10.1029/GL014i010p01027 (1987).

[5] Mirinova, I. A. et al. Ionization of the Polar Atmosphere by Energetic Electron Precipitation Retrieved From Balloon Measurements. *Geophys. Res. Lett*. **46**, 2, 990-996 https://doi.org/10.1029/2018GL079421 (2019).

[6] Funke, B. et al. HEPPA-II model–measurement intercomparison project: EPP indirect effects during the dynamically perturbed NH winter 2008–2009. *Atmos. Chem. Phys.,* **17**, 5, 3573–3604 https://doi.org/10.5194/acp-17-3573-2017 (2017).

[7] Randall, C.E. et al. Simulation of energetic particle precipitation effects during the 2003–2004 Arctic winter. *J. Geophys. Res. Space Phys*. **120**, 6, 5035-504 ,https://doi.org/10.1002/2015JA021196 (2016).

[8] Gonzales, W.D. et al. What is a geomagnetic storm? *J. Geophys. Res.* **99**, A4, 5771-5792 doi:10.1029/93JA02867 (1994).

[9] Baker, D. N., et al., Space Weather Effects in the Earth's Radiation Belts, *Space Sci. Rev.*, **214**, 17, https://doi.org/10.1007/s11214-017-0452-7 (2018).

[10] Schulz, M. & Lanzerotti, L.J. Particle Diffusion in the Radiation Belts in Physics and Chemistry in Space (ed. vol. 7, Roederer, J.G.)(Springer-Verlag, New York) https://doi.org/10.1007/978-3-642-65675-0 (1974).

[11] Imhof, W.L., Reagan, J.B. & Gaines, E.E., Fine-scale spatial structure in the pitch angle distributions of energetic particles near the midnight trapping boundary. *J. Geophys. Res. Space Phys.* **82**, 32, 5215-5221 https://doi.org/10.1029/JA082i032p05215 (1977).

[12] Shprits, Y.Y., Subbotin, D. & Binbin, N., Evolution of electron fluxes in the outer radiation belt computed with the VERB code. *J. Geophys. Res., Space Phys.* **114**, A11 https://doi.org/10.1029/2008JA013784 (2009).

[13] Glauert, S. A., Horne, R.B., & Meredith, N.P. Three-dimensional electron radiation belt simulations using the BAS Radiation Belt Model with new diffusion models for chorus, plasmaspheric hiss, and lightning-generated whistlers. *J. Geophys. Res., Space Phys.*, **119**, 1, 268-289 https://doi.org/10.1002/2013JA019281 (2014).

[14] Khazanov, G. V., Glocer, A. & Chu, M. The Formation of Electron Heat Flux in the Region of Diffuse Aurora. *J. Geophys. Res., Space Phys.* **125**, 8, https://doi.org/10.1029/2020JA028175 (2020).

---

[15] Marshall, R. A., & Bortnik, J. Pitch Angle Dependence of Energetic Electron Precipitation: Energy Deposition, Backscatter, and the Bounce Loss Cone. *J. Geophys. Res., Space Phys.* **123**, 3, 2412-2423 https://agupubs.onlinelibrary.wiley.com/doi/full/10.1002/2017JA024873 (2018).

[16] Angelopoulos, V., et al. The ELFIN Mission, *Space Sci. Rev.* **216**, 103 https://doi.org/10.1007/s11214-020-00721-7 (2020).

[17] Mayaud, P. N. Derivation, meaning, and use of geomagnetic indices. Geophys. Monogr. Ser. **22**, 154 pp., American Geophysical Union, doi:10.1029/GM022 (1980).

[18] http://wdc.kugi.kyoto-u.ac.jp/

[19] Yokoyama, N., Kamide, Y., & Miyaoka, H., The size of the auroral belt during magnetic storms. *Ann. Geophys.* **16**, 566-573 https://doi.org/10.1007/s00585-998-0566-z (1998).

[20] Angelopoulos, V., et al., The Space Physics Environment Data Analysis System (SPEDAS). *Space Sci. Rev.* **215**, 9 https://doi.org/10.1007/s11214-018-0576-4 (2019).

Supplementary Materials for:

Atmospheric scattering of energetic electrons from near-Earth space

V. Angelopoulos[1*], E. Tsai[1], C. Wilkins[1], X.-J. Zhang[1], A. V. Artemyev[1], J. Liu[1], A. Runov[1], L. Iglesias[1], D. L. Turner[2], R. J. Strangeway[1], R. E. Wirz[3], W. Li[4], L. Adair[1,5], R. P. Caron[1], M. Chung[2], P. Cruce[6], E. Grimes[1], K. Hector[7], M. J. Lawson[1], D. Leneman[1], E. V. Masongsong[1], A. Norris[1], C. L. Russell[1], C. Shaffer[8], J. Wu[1], S. Jha[1,9], J. King[1,9], S. Kumar[1,10], K. Nguyen[1,3], M. Nguyen[1,11], A. Palla[1,9], A. Roosnovo[1,10], E. Xie[1,11], R. Yap[1,12], C. Young[1,9], J. B. Blake[13], N. Adair[5], M. Allen[14], M. Anderson[15], M. Arreola-Zamora[1,14], J. Artinger[1,10], J. Asher[2], D. Branchevsky[13], M. R. Capitelli[5], R. Castro[7,9], G. Chao[3,16], N. Chung[17], M. Cliffe[18], K. Colton[19], C. Costello[20], D. Depe[11], B. W. Domae[11], S. Eldin[11], L. Fitzgibbon[8], A. Flemming[14], I. Fox[3], D. M. Frederick[5], A. Gilbert[11], A. Gildemeister[14], A. Gonzalez[9], B. Hesford[21], R. Krieger[22], K. Lian[14], J. Mao[23], E. McKinney[24], J. P. Miller[9], M. Nuesca[9], E. S. Y. Park[25], C. E. Pedersen[3], Z. Qu[3], R. Rozario[18], E. Rye[11], R. Seaton[1], A. Subramanian[14], S. R. Sundin[8], A. Tan[26], W. Turner[10], A. J. Villegas[10], M. Wasden[3], G. Wing[9], C. Wong[10], A. Zarifian[21], G. Y. Zhang[27]

Affiliations:

1 Earth, Planetary, and Space Sciences Department, and Institute of Geophysics and Planetary Physics, University of California, Los Angeles, CA 90095
2 Johns Hopkins University Applied Physics Laboratory, Laurel, Maryland 20723
3 Mechanical and Aerospace Engineering Department, Henry Samueli School of Engineering, University of California, Los Angeles, CA 90095
4 Department of Astronomy and Center for Space Physics, Boston University, Boston, MA 02215
5 Millenium Space Systems, El Segundo, CA 90245
6 Apple Inc., Cupertino, CA 95014
7 Raytheon Space and Airborne Systems, El Segundo, CA 90245
8 Tyvak Nano-Satellite Systems, Inc., Irvine, CA 92618
9 Computer Science Department, Henry Samueli School of Engineering, University of California, Los Angeles, CA 90095
10 Physics and Astronomy Department, University of California, Los Angeles, CA 90095
11 Electrical and Computer Engineering Department, Henry Samueli School of Engineering, University of California, Los Angeles, CA 90095
12 Mathematics Department, University of California, Los Angeles, CA 90095
13 The Aerospace Corporation, El Segundo, CA 90245
14 Northrop Grumman Aerospace Systems, Redondo Beach, CA 90278
15 Lucid Motors, Newark, CA 94560
16 Boeing, El Segundo, CA 90245
17 Tesla, Palo Alto, CA 94306
18 SpaceX, Hawthorne, CA 90250
19 Planet Labs, San Francisco, CA 94107
20 NovaSignal, Los Angeles, CA 90064
21 Jet Propulsion Laboratory, Pasadena, CA 91109
22 Mercedes-Benz Research and Development North America, Long Beach, CA 90810
23 Epic Systems Corporation, Verona, WI 53593
24 California State Polytechnic University, Pomona, CA 91768
25 Economics Department, University of California, Los Angeles, CA 90095
26 Experior Laboratories, Oxnard, CA 93033
27 Qualcomm, San Diego, CA 92121

[*]Correspondence to: vassilis@ucla.edu

This file includes:

Methods

M1. Statistical significance of loss cone fluxes and their ratios

Although the EPDE's side-penetrating radiation is insignificant thanks to high shielding and coincidence logic[16], counting statistics must still be utilized to guarantee a robust signal-to-noise ratio. Poisson statistics govern detector counts; the relative error dQ/Q of any quantity Q proportional to the count rate (such as the energy flux) is $1/\sqrt{N}$, where N is the total number of counts in the measurement. To determine it, we obtain the net raw number of counts, N, that contributed to each measurement (e.g., Q may be the average energy flux in two or three sectors within the loss cone) and carry this information in the data processing along with the measurement. For derived products, such as integral or average energy flux, we then use error propagation formulas to compute the error for each quantity at every time step. An error tolerance of $dQ/Q < 50\%$ for a data point would thus require that at least N=4 counts contributed to that measurement of Q.

Electronic noise, which also exists in the measurements, can be recognized as random, low-flux pixels at high energies in the energy spectra in Figures 1d-f (and also in Extended Data Figures 1C-E and 2C-E). Most often each pixel corresponds to one count. This electronic noise is readily eliminated by the aforementioned criterion $dQ/Q<50\%$ when applied to derived products, such as flux ratio spectrograms (Figures 1g-i; Extended Data Figures 1F-H and 2F-H), or to the time-series ratios of directional broad-energy channels HiE and LoE. The very low contribution of electronic noise to the measurement can be readily assessed from data collected at the magnetic equator, below the inner belt, when no geophysical signal is present. From such data we determined that electronic noise contributes $f_{n,HiE}= 3.48\text{x}10^3$

keV/cm^2s·str·MeV and $f_{n,LoE}$= 2.74x10^3 keV/cm^2s·str·MeV to the energy flux in the two energy channels, HiE and LoE, respectively. We subtracted this noise from measurements in our statistics if they had not already been subjected to the counting statistics threshold (e.g., dQ/Q < 50% or similar) that automatically rejects electronic noise.

To demonstrate that noise does not affect our loss-cone measurements, we show in Extended Data Figure 3A the energy flux spectra as a function of pitch angle, averaged over 11 spins during the moderate precipitation interval, 13:12:17-13:12:50 UT in Figure 1. A pitch-angle $\alpha=0^o$ corresponds to downgoing electrons, and vertical long-dashed lines denote the loss cone (short-dashed lines denote the anti-loss cone). The dashed colored lines, mirror-images of the downgoing fluxes about the pitch angle, $\alpha=0^o$, enable direct comparison of upgoing (solid) and downgoing (dashed) lines at the same energy (color) in the raw data. The upgoing-to-downgoing flux ratio in the loss cone thus can be estimated from Extended Data Figure 3A to be about 30% at low energies (warm colors, higher fluxes) and to approach 100% at high energies (cold colors, lower fluxes). The horizontal dashed line represents a flux corresponding to ~10 counts, i.e., a relative error of dQ/Q ~ 30% (here Q is the energy flux in each sector, centered at one distinct pitch angle). Below that horizontal dashed line, the data points fluctuate considerably, consistent with statistical noise, but above it, the data points vary smoothly in pitch angle. Our conclusions regarding ratio evolution are drawn from fluxes that are well above the horizontal dashed line, based on dQ/Q criteria, and therefore are statistically significant.

Upgoing-to-perpendicular and upgoing-to-downgoing ratios of flux averages derived from Extended Data Figure 3, Panel A, are plotted in Panel C; for convenience, these are plotted on the left and right halves of the panel, respectively. Only the ratios with $dQ/Q<30\%$ are plotted; the absolute error based on the number of counts for each ratio is demarcated above and below each point by a vertical bar. This restriction on counting statistics also eliminates electronic noise, as discussed earlier. The upgoing-to-downgoing ratio of the average fluxes (right half of Panel B) exhibits the behavior already surmised from the raw data in Panel A: within the loss cone, it is low at low energies (warm colors) but it approaches 100% at increasing energies (cold colors). This behavior is also consistent with the plots of instantaneous (one per spin) flux ratios in Figure 1i;, Figure 1l,m; and their equivalent panels in Extended Figures 1 and 2. It shows that statistical or electronic noise has been duly eliminated and does not interfere with our ability to obtain statistically significant fluxes and flux ratios.

M2. Purity of loss-cone flux

For each sector in spin phase, the detector's finite geometric field of view (22^{o}) and finite accumulation time in spin phase (22.5^{o}) result in a full width of 44.5^{o} and full width at half-max of the contribution to the sector's flux of 33.25^{o}. We rotate the two-dimensional angular detector view (originally in polar and azimuthal angles in spacecraft geometric coordinates) into field-aligned (pitch-angle and gyro-phase) coordinates and collapse it into 1D pitch-angle space at every spin. This results in a smaller full width in pitch-angle space (as low as 22^{o}). We ensure that the viewing windows of the sectors we rely upon to produce the net loss-cone flux are all inside the loss cone, up to the vertices of those windows.

To demonstrate the result of this mapping process, we show the fields of view of all sectors during all spins in Extended Data Figure 3, Panel B (11 spins x 16 sectors are overplotted in that panel, but the spin-to-spin variation is imperceptible, as the magnetic field direction does not change appreciably in the time interval considered). The full width is the thin horizontal line, and the full width half-max is the thick horizontal line. The detector measures particles arriving from the exact edge of the thick line for only 50% of the full sector accumulation time (as opposed to 100% at the center). The contribution to the sector's average flux from pitch angles outside the thick line decreases linearly to 0% at the pitch angles at two edges of the thin line.

For a bin's measurements to be counted in the upgoing or downgoing flux, we require that its full width be in the nominal loss cone (or anti-loss cone). Any contribution of the loss cone's finite edge to the total flux is therefore attenuated by the limited time the detector spends in that direction (<1/32 of the sector's flux contribution arises from a 5.6^{o} angle next to its edge) and by the contribution of other sectors well inside the loss cone. In Extended Data Figure 3, Panels B and C, four sectors contribute to the downgoing flux and four to the upgoing flux, the four closest to $\alpha=0^{o}$ and $\alpha=180^{o}$, respectively. Their upgoing-to-perperpendicular and upgoing-to-downgoing ratios exhibit a smooth variation with α. Our conclusions on ratios drawn from those four sectors are consistent with the behavior of the two sectors with edges farthest from the loss cone ($>15^{o}$).

Extended Data Figure 1

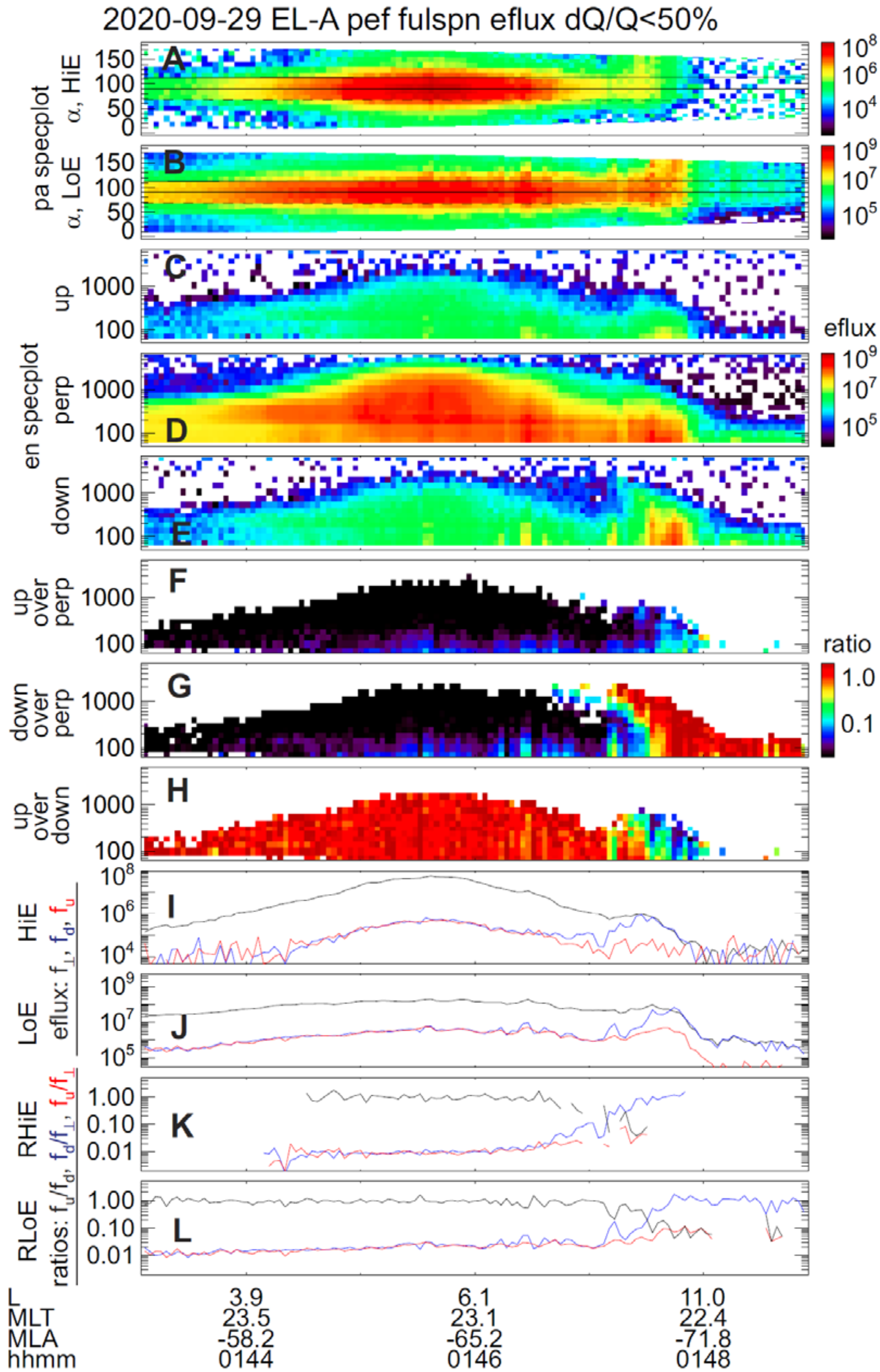

Extended Data Figure 1 | ELFIN-A nonstorm-time, nightside crossing of the outer radiation belt and auroral zone. Format of Panels A-L is identical to that of Panels b-m in Figure 1. (**A-B**) Pitch-angle spectrograms of differential directional (broad) electron energy flux channels HiE and LoE (430-5800keV and 50-430keV, respectively). Upper solid and bottom dashed horizontal lines: loss cone ($\alpha=\alpha_{LC}$) and anti-loss cone ($\alpha=180^{o}-\alpha_{LC}$); middle solid line: $\alpha=90^{o}$. (**C**-**E**) Energy-time spectrograms of upgoing, trapped, and downgoing electron energy flux, respectively. (**F**-**H**) Energy-time spectrograms of upgoing-to-perpendicular (up-to-perp, $f_u/f_\perp$), downgoing-to-perpendicular (down-to-perp, $f_d/f_\perp$), and upgoing-to-downgoing (f_u/f_d) electron energy flux, respectively. Note in the $f_d/f_\perp$ spectrogram the clear decrease in the minimum energy of $f_d/f_\perp$~1 with increasing latitude, a characteristic signature of precipitation by field-line scattering[11]. (**I**-**J**) Energy flux in channels HiE and LoE, respectively (black: $f_\perp$; blue: f_d; red: f_u). (**K**-**L**) Ratios of energy flux in channels HiE and LoE, respectively (black: f_u/f_d; blue: $f_d/f_\perp$; red: $f_u/f_\perp$). Annotations denote L-shell (L), dipole magnetic local time (MLT), dipole magnetic latitude (MLA), and Universal Time (UT).

Extended Data Figure 2

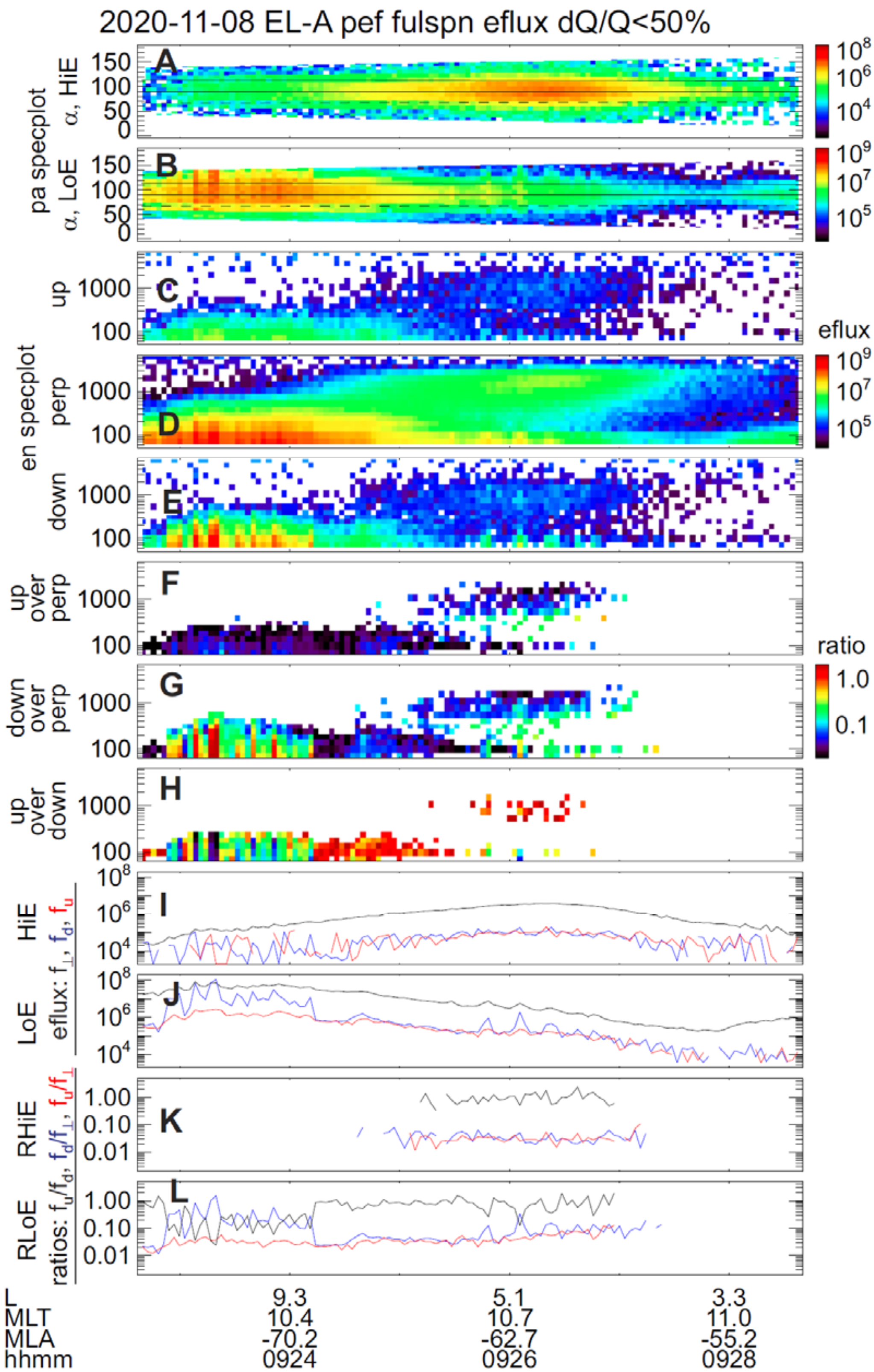

Extended Data Figure 2 | ELFIN-A dayside crossing of the outer radiation belt and auroral zone during the late recovery phase of a small storm. Format of Panels A-L is identical to that of Panels b-m in Figure 1. (**A-B**) Pitch-angle spectrograms of differential directional (broad) electron energy flux channels HiE and LoE (430-5800keV and 50-430keV, respectively). Upper solid and bottom dashed horizontal lines: loss cone ($\alpha=\alpha_{LC}$) and anti-loss cone ($\alpha=180^o-\alpha_{LC}$); middle solid line: $\alpha=90^o$. (**C**-**E**) Energy-time spectrograms of upgoing, trapped, and downgoing electron energy flux, respectively. (**F**-**H**) Energy-time spectrograms of upgoing-to-perpendicular (up-to-perp, $f_u/f_\perp$), downgoing-to-perpendicular (down-to-perp, $f_d/f_\perp$), and upgoing-to-downgoing (f_u/f_d) electron energy flux, respectively. (**I**-**J**) Energy flux in channels HiE and LoE, respectively (black: $f_\perp$; blue: f_d; red: f_u). (**K**-**L**) Ratios of energy flux in channels HiE and LoE, respectively (black: f_u/f_d; blue: $f_d/f_\perp$; red: $f_u/f_\perp$). Annotations denote L-shell (L), dipole magnetic local time (MLT), dipole magnetic latitude (MLA), and Universal Time (UT).

Extended Data Figure 3

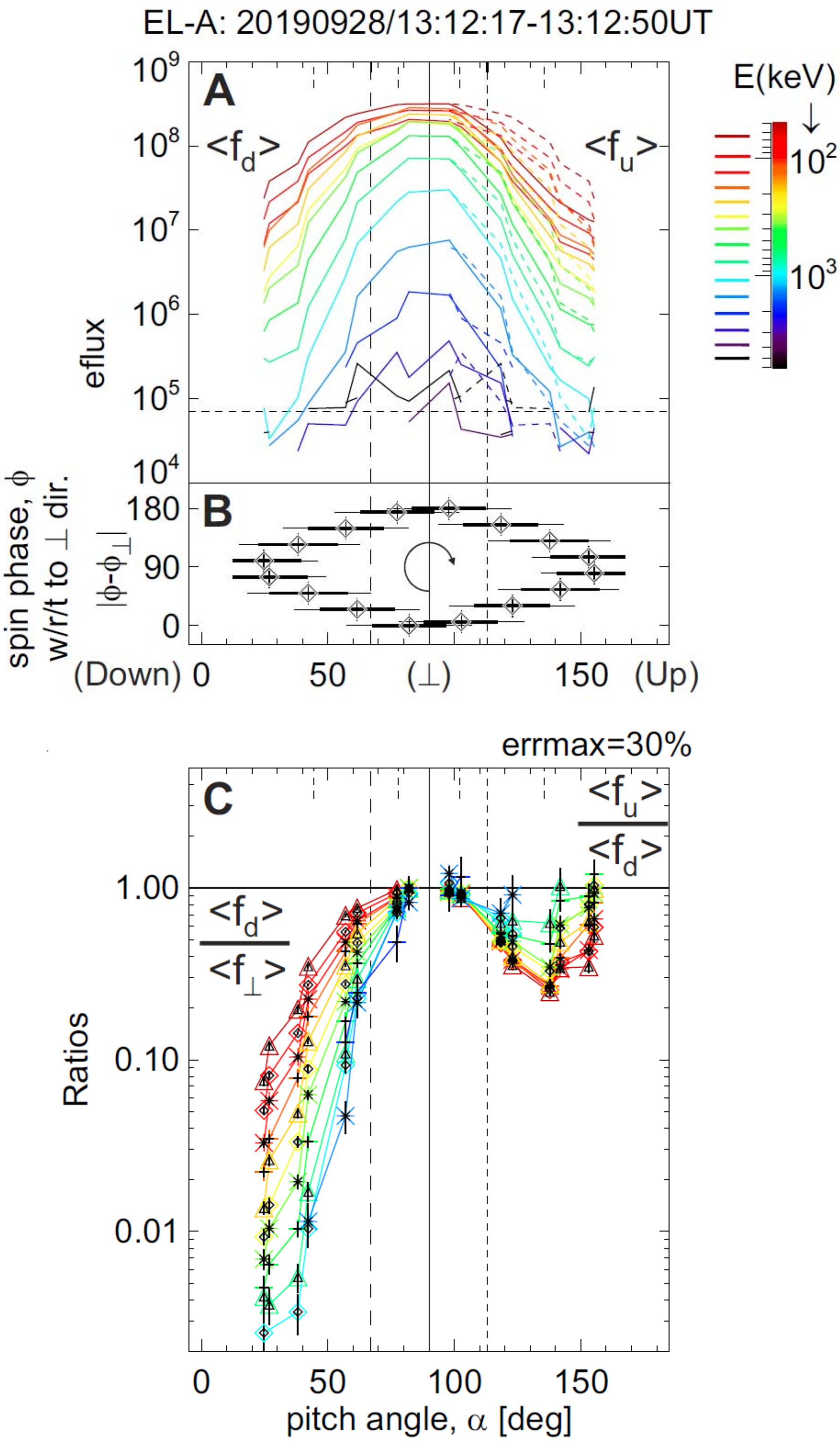

Extended Data Figure 3 | Veracity of loss-cone fluxes and their ratios. (**A**) Pitch-angle spectra of average fluxes from 11 spins (time interval indicated atop) for EPDE's logarithmically-equidistant energy channels from low (warmer colors) to high (colder colors) for ELFIN-A. Vertical lines denote pitch angles α=90^o (middle, solid), the loss cone (α=α_{LC}, left, long-dashed), and the anti-loss cone (α=180^o-α_{LC}, right, short-dashed). Dotted colored lines denote downgoing fluxes mirrored about pitch-angle α=0^o (i.e., plotted versus the supplementary of their pitch angles) for easy comparison with upgoing fluxes at the same energy (solid colored lines). The limits used to select field-aligned and perpendicular pitch-angle sector centers are four short dashed lines hanging down from the top of the panel. Two are 22.5^o closer to the field-line direction than the loss and the anti-loss cone, respectively; two are 11.25^o closer to perpendicular than the loss and the anti-loss cone, respectively. (**B**) Sector pitch angle, α (center, diamond), and width (acceptance angle, horizontal bar) as function of the sector center's spin-phase absolute distance from the (ascending) direction perpendicular to the magnetic field, $|\phi-\phi_\perp|$. The arrow in the centered circle denotes the direction of the detector's rotation in time during the spin. The thin horizontal bar centered at the diamond denotes the sector's pitch-angle full-width full max; the thick bar denotes its full-width half max. (**C**) Pitch-angle spectra of ratios of average fluxes for each energy channel (color) as determined from Panel A. The down-to-perpendicular ratio is on the left (0^o<α<90^o); the upgoing-to-downgoing ratio is on the right (90^o<α<180^o). Vertical dashed lines are same as in Panel A. Vertical bars at each point demarcate $\pm$dr, the absolute error value for each ratio r. Only points with dr/r<30% are shown.

Extended Data Figure 4 (Rotate clockwise by 90^{o})

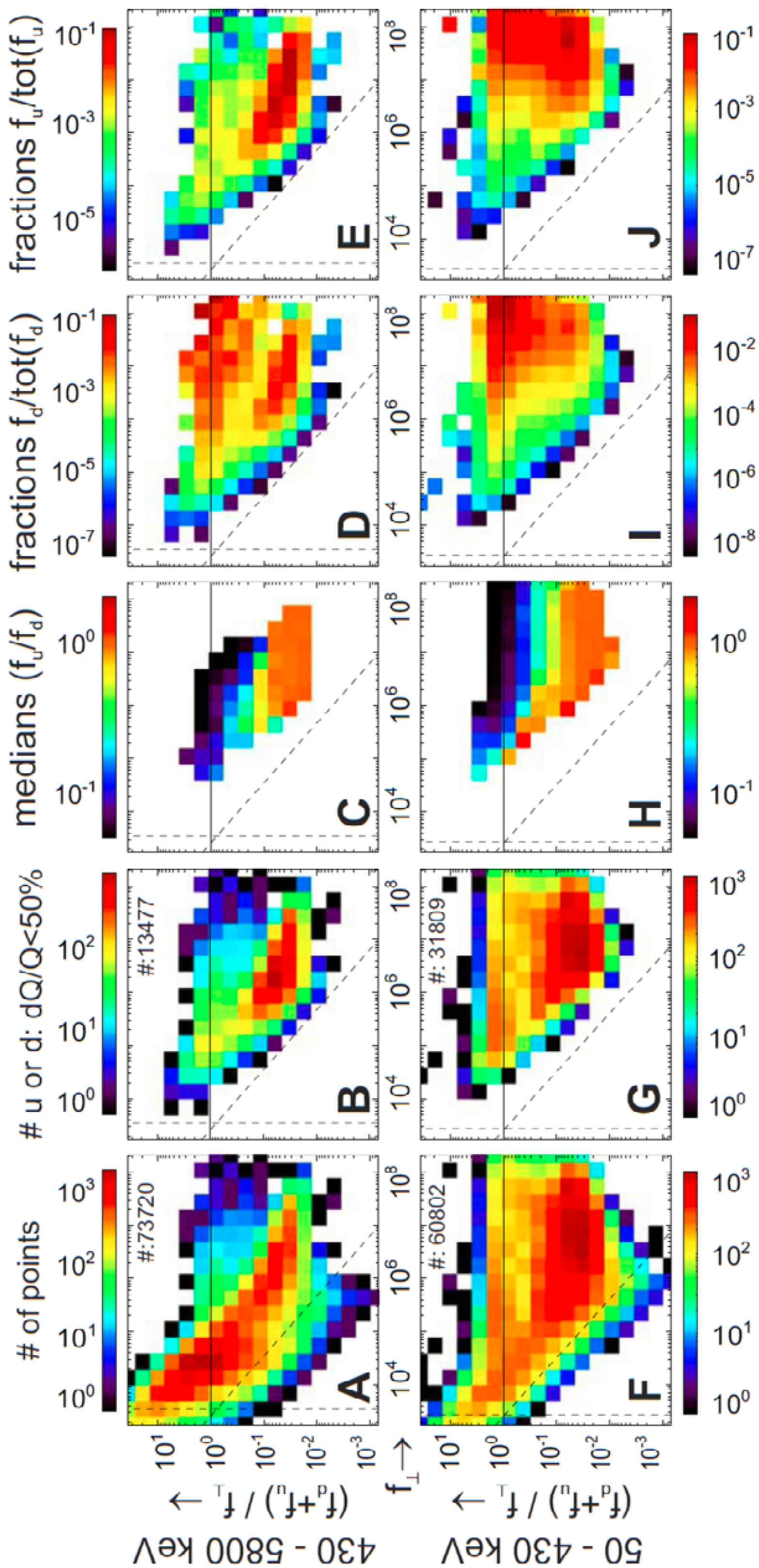

Extended Data Figure 4 (Rotate clockwise by 90°) | Statistical distribution of points, flux, and flux ratios. All panels show distributions in two-dimensional (2D) space ($f_\perp$, $(f_d+f_u)/f_\perp$), where $f_\perp$ is the differential directional energy flux (in keV/cm^2 s str MeV) measured near α=90° (trapped flux, perpendicular, $\perp$, to the **B** field) and (f_d+f_u) is the upward-plus-downward flux (in the loss cone and anti-loss cone). Top and bottom rows are for the HiE and LoE channels (430-5800keV and 50-430keV), respectively. Vertical dashed lines are the electronic noise flux values, f_{n_HiE} and f_{n_HiE}, for the HiE and LoE channels, respectively; diagonal dashed lines are the electronic noise divided by $f_\perp$. Measurements to the left of these lines are consistent with electronic noise. (**A**, **F**) Distribution of data in the database used (number of samples, #, indicated as an insert). (**B**, **G**) Distribution of data with statistically significant upgoing or downgoing fluxes (df/f<50%), which additionally eliminates samples corresponding to electronic noise. Note that most low $f_\perp$ points have been eliminated from flux ratios in these and remaining 2D panels in the figure; averages computed from these statistically significant samples are intended to be representations of the total measured flux for the purpose of computing flux ratios, not the absolute flux. (Absolute flux depends on absolute detector efficiency, which has not yet been fully evaluated, but is not critical for this study). Panels (B, G) are the 2D versions of the PDFs for HiE and LoE in Figure 3a. (**C**, **H**) Distribution of medians of ratios f_d/f_u for statistically significant fluxes. As $(f_d+f_u)/f_\perp$ decreases, most medians increase from a few % to ~100% for most $f_\perp$ values, particularly in cells with large numbers of points in Panels B and G. Panels (C, H) are the 2D versions of the median f_u/f_d lines in Figure 3a. (**D**, **I**) Distribution of the relative contribution to the total downgoing flux, f_d, by each cell in this 2D space. Two clusters of points with very weak dependence on $f_\perp$ are evident: one near $(f_d+f_u)/f_\perp$~0.04, which we attributed to atmospheric scattering of trapped particles, and another near $(f_d+f_u)/f_\perp$~1, which we attributed to magnetospheric scattering. These are the 2D versions of the line plots for HiE and LoE in Figure 3c. (**E**, **J**) Same as in Panels (D, I) except for the upgoing flux, f_u. The same two main populations are evident here, as well. These are the 2D versions of the line plots for HiE and LoE in Figure 3b.

Extended Data Table 1

Average Directional Electron Fluxes† and their Ratios							
All data in 3<L<7							
MLT	Energy [keV]	r=<f_u>/<f_d>	<f_d>/<$f_\perp$>	<$f_\perp$>	[Units]	Inferred‡ Ratios: x=2fa/fm	Inferred‡ Ratios: R=2fa/(2fa+fm)
Night	LoE: 50-430	9.3%	35.1%	1.65E+07	keV/cm^2 s str MeV (Differential Directional Energy Flux)		
Night	HiE: 430-5800	27.8%	8.3%	1.50E+06			
Day	LoE: 50-430	21.4%	16.3%	6.13E+06			
Day	HiE: 430-5800	81.2%	4.9%	5.55E+05			
Night+Day, Residence-time Norm'ed	LoE: 50-430	11.1%	30.0%	1.13E+07			
Night+Day, Residence-time Norm'ed	HiE: 430-5800	37.5%	7.4%	1.03E+06		120%	55%
Night+Day, Residence-time Norm'ed	50-5800 (Integral)	17.4%	17.3%	9.83E+06	keV/cm^2 s str	42%	30%
D_{ST} < -20nT in 3<L<7							
MLT	Energy [keV]	r=<f_u>/<f_d>	<f_d>/<$f_\perp$>	<$f_\perp$>	[Units]	Inferred‡ Ratios: x=2fa/fm	Inferred‡ Ratios: R=2fa/(2fa+fm)
Night	LoE: 50-430	8.5%	35.7%	3.27E+07	keV/cm^2 s str MeV (Differential Directional Energy Flux)		
Night	HiE: 430-5800	22.7%	7.8%	2.37E+06			
Day	LoE: 50-430	23.2%	12.5%	1.16E+07			
Day	HiE: 430-5800	90.4%	3.9%	5.96E+05			
Night+Day, Residence-time Norm'ed	LoE: 50-430	10.2%	29.6%	2.21E+07			
Night+Day, Residence-time Norm'ed	HiE: 430-5800	30.3%	7.0%	1.48E+06		87%	46%
Night+Day, Residence-time Norm'ed	50-5800 (Integral)	13.8%	18.6%	1.64E+07	keV/cm^2 s str	32%	24%

†Noise subtracted: $f_{n,HiE}$=3.48 10^3, $f_{n,LoE}$=2.74 10^3 [keV/cm^2 s str MeV] ‡where R=x(x+1); r=x/(x+2)

Extended Data Table 1 | Differential and integral directional energy fluxes and ratios for the outer radiation belt (3<L<7) under all geomagnetic conditions (top) and for active (D_{ST}<-20nT) times (bottom). Ratios of time averages rather than medians of ratios have been used to accurately characterize total energy flux ratios. The combination of Night and Day ratios was determined directly from the numbers above them, assuming equal satellite residence time in the dayside and the nightside. The bottom row, which represents the integral directional energy flux channel (50-5800keV), was computed directly from the rows above it. f_u and f_d are upgoing and downgoing fluxes, <> represent averages, and f_a and f_m are the measured contributions to precipitation from atmospheric scattering and magnetospheric scattering. The ratios x and R are the inferred net contributions to precipitation from atmospheric scattering relative to magnetospheric scattering and relative to the total precipitation, respectively.